

A Droplet-Based High-Throughput SERS Platform on a Droplet-Guiding-Track-Engraved Superhydrophobic Substrate

Sera Shin, Jaehong Lee, Sanggeun Lee, Hyunchul Kim, Jungmok Seo, Dayeong Kim, Juree Hong, Soonil Lee, and Taeyoon Lee*

A novel droplet-based surface-enhanced Raman scattering (SERS) sensor for high-throughput real-time SERS monitoring is presented. The developed sensors are based on a droplet-guiding-track-engraved superhydrophobic substrate covered with hierarchical SERS-active Ag dendrites. The droplet-guiding track with a droplet stopper is designed to manipulate the movement of a droplet on the superhydrophobic substrate. The superhydrophobic Ag dendritic substrates are fabricated through a galvanic displacement reaction and subsequent self-assembled monolayer coating. The optimal galvanic reaction time to fabricate a SERS-active Ag dendritic substrate for effective SERS detection is determined, with the optimized substrate exhibiting an enhancement factor of 6.3×10^5 . The height of the droplet stopper is optimized to control droplet motion, including moving and stopping. Based on the manipulation of individual droplets, the optimized droplet-based real-time SERS sensor shows high resistance to surface contaminants, and droplets containing rhodamine 6G, Nile blue A, and malachite green are successively controlled and detected without spectral interference. This noble droplet-based SERS sensor reduces sample preparation time to a few seconds and increased detection rate to $0.5 \mu\text{L s}^{-1}$ through the simple operation mechanism of the sensor. Accordingly, our sensor enables high-throughput real-time molecular detection of various target analytes for real-time chemical and biological monitoring.

1. Introduction

Raman spectroscopy is a well-known analytic tool based on the inelastic scattering of a photon from a molecule that

S. Shin, J. Lee, S. Lee, H. Kim, Dr. J. Seo,^[+] D. Kim, Dr. J. Hong, S. Lee, Prof. T. Lee
School of Electrical and Electronic Engineering
Yonsei University
50 Yonsei-ro, Seodaemun-Gu
Seoul 03722, Republic of Korea
E-mail: taeyoon.lee@yonsei.ac.kr



^[+]Present address: Department of Medicine, Biomaterials Innovation Research Center, Brigham and Women's Hospital, Harvard Medical School, Cambridge, MA 02139, USA; Harvard-MIT Division of Health Sciences and Technology, Massachusetts Institute of Technology, 77 Massachusetts Avenue, Cambridge, MA 02139, USA

DOI: 10.1002/sml.201602865

provides information about molecular vibrations, which can be used for molecular detection, identification, and diagnosis.^[1] Over the last few decades, surface-enhanced Raman scattering (SERS) techniques, in which the Raman signals are significantly enhanced based on strong electromagnetic fields amplified by noble metal nanostructures, have been developed, demonstrating powerful analytic performance, including superb sensitivity for the detection of molecules.^[2–4] SERS-based detection has been explored in a broad range of research fields as an attractive and promising spectroscopic technique. In particular, microfluidic devices coupled with SERS have been recently demonstrated for in situ monitoring of chemical reactions and detection of analytes.^[5–7] To obtain SERS-integrated microfluidic devices, SERS-active metallic nanostructures fabricated by various methods, such as electromigration,^[8] E-beam lithography,^[9,10] Langmuir–Blodgett techniques,^[11] laser direct writing,^[12,13]

plasma etching,^[7] and a polyol method,^[6] have been intensively investigated in closed-channel microfluidic devices. However, the SERS substrates fabricated via the aforementioned methods inside the microfluidic channel have limited abilities owing to the destruction and contamination of metallic nanostructures in the fluid channel, leading to imprecise detection of analytes. For instance, Leem et al. patterned SERS-active Ag nanostructures in a microfluidic channel using a polyol method and then, conducted real-time SERS measurements with various concentrations of analyte;^[6] however, the intensity of the SERS signal did not correspond to the concentration of the injected solution owing to destruction of the fabricated Ag nanostructures. Therefore, the significant limitations of the existing SERS-integrated microfluidic devices should be overcome.

On the other hand, open-channel microfluidic devices have attracted a considerable amount of interest as an advanced microfluidic platform owing to several advantages in terms of simple design, low cost manufacture, and efficient control of small-volume droplets.^[14–16] In particular, droplet-based open-channel microfluidic devices that exhibit water-repellent properties with a negligible friction force between the droplet and the surface have strong merits for the efficient manipulation of droplets without any surface contamination.^[16,17] Therefore, droplet-based open-channel microfluidic devices coupled with SERS that have a high resistance to surface contaminants have great potential for overcoming the limitations of the previous SERS-integrated microfluidic devices in terms of destruction and contamination of the SERS-active metallic nanostructures.

Herein, we demonstrate a novel approach for a droplet-based real-time SERS sensor based on a superhydrophobic guiding track, which enables individual manipulation and SERS measurement of analyte droplets without any loss or surface contamination, as an advanced functional open-channel microfluidic device. SERS-active metallic nanostructures were formed on the predefined Cu plate via an electroless galvanic displacement reaction between Ag and Cu, and extreme water-repellent properties were achieved through surface modification with a low-surface-energy material. Droplet motions on the superhydrophobic SERS-active substrate were successfully controlled along the

predefined guiding track with a droplet stopper owing to the water-repellent properties of the substrate and gravitational force. The transportation of successive droplets to the laser spot for SERS measurement was achieved via a collision process between droplets using the droplet stopper, without additional droplet-control equipment. To the best of our knowledge, this is the first attempt to overcome the limitations of conventional SERS-integrated microfluidic devices, which include slow detection rates and surface contamination. Most importantly, our droplet-based SERS sensor takes advantages of the effective manipulation of successive droplets, as well as the fact that additional cleaning processes are not required for successive SERS measurements. Due to these advantages, high-throughput SERS monitoring could be achieved by overcoming the aforementioned limitations of conventional SERS-integrated microfluidic devices. Using this novel sensor, successive SERS measurements were successfully achieved for droplets containing low concentrations (up to 10^{-6} M) of rhodamine 6G (R6G), Nile blue A (NBA), and malachite green (MG) with a detection rate of $0.5 \mu\text{L s}^{-1}$, higher than that of a closed-channel microfluidic device ($\approx 0.2 \mu\text{L s}^{-1}$) without a cleaning process, enabling high-throughput real-time SERS monitoring.

2. Results and Discussion

The development of a droplet-based real-time SERS sensor involves three main steps: (i) engraving of a droplet-guiding track on a Cu plate, (ii) fabrication of superhydrophobic Ag structures on the engraved plate through the formation of Ag nanostructures and a self-assembled monolayer coating (Figure 1a), and (iii) realization of droplet-based real-time SERS sensor on the fabricated superhydrophobic plate (Figure 1b). In particular, the development of a superhydrophobic substrate is fundamental for droplet-based real-time SERS sensors (Figure 1a-ii). In this step, the superhydrophobic Ag structures were fabricated through an electroless galvanic displacement reaction and self-assembled monolayer coating with 1*H*,1*H*,2*H*,2*H*-perfluorodecanethiol (PFDT). Because the standard electrochemical potential of Cu (0.34 V) is lower than that of Ag (0.80 V), Ag ions could

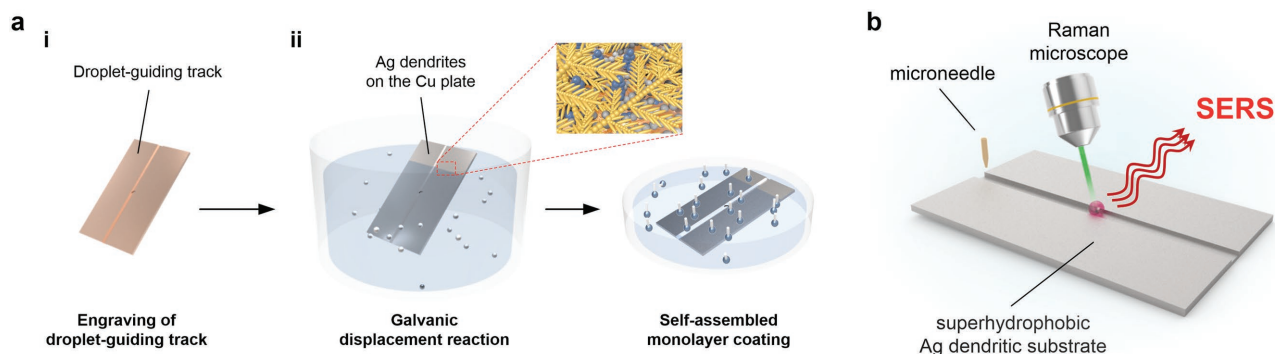


Figure 1. a) Fabrication of superhydrophobic Ag dendritic substrates: (i) engraving of a droplet-guiding track on a Cu plate and (ii) galvanic displacement reaction of the Cu plate, followed by coating with a self-assembled monolayer. b) Schematic illustration of the droplet-based real-time SERS sensor realized on the superhydrophobic Ag dendritic substrate.

easily receive electrons from the Cu plate and be reduced when the Cu plate was immersed in AgNO_3 aqueous solution.^[18] Subsequently, further chemical modification by coating with PFDT was used to lower the surface energy of the Ag structures.

Figure 2a–e exhibits typical scanning electron microscopy (SEM) images of the Ag dendritic micro-/nanostructures fabricated on Cu plates as a function of immersion time during the electroless galvanic displacement reaction. When the Cu plate was immersed in AgNO_3 aqueous solution, the chemical reaction between the metals occurred immediately. When provided with electrons from the Cu plate, Ag ions were reduced to Ag particles and randomly deposited during the first short immersion time of 10 s (Figure 2a). As the displacement reaction proceeded, evolution of the morphology of the initially deposited Ag nanoparticles occurred (Figure 2b). Further reaction tends to occur preferentially at energetically favorable Ag nanoparticles deposited on the Cu plate. When

the Cu plate was immersed for more than 1 min, trunks and short branches of Ag dendrites began to grow from the sites (Figure 2c,d).^[19–22] After 10 min, hierarchical structures composed of Ag nanoparticles, branches, and leaves were fabricated (Figure 2e). A schematic illustration of each growth step of the Ag dendritic hierarchical structures is shown in Figure S1 of the Supporting Information.

X-ray diffraction (XRD) measurements were carried out to investigate the chemical composition of the fully grown Ag dendritic structures. The four diffraction peaks detected at 38.20° , 44.32° , 64.52° , and 77.56° in the XRD pattern match well with the standard pattern of Ag face-centered cubic (fcc) structures (JCPDS No. 04-0783) and correspond to characteristic diffractions from the (111), (200), (220), and (311) planes of Ag fcc structures, respectively (Figure 2f).^[21,23] The strong and sharp diffraction peaks observed for the as-prepared substrate indicate the high crystallinity of the Ag dendritic structures. Meanwhile, the three diffraction peaks detected

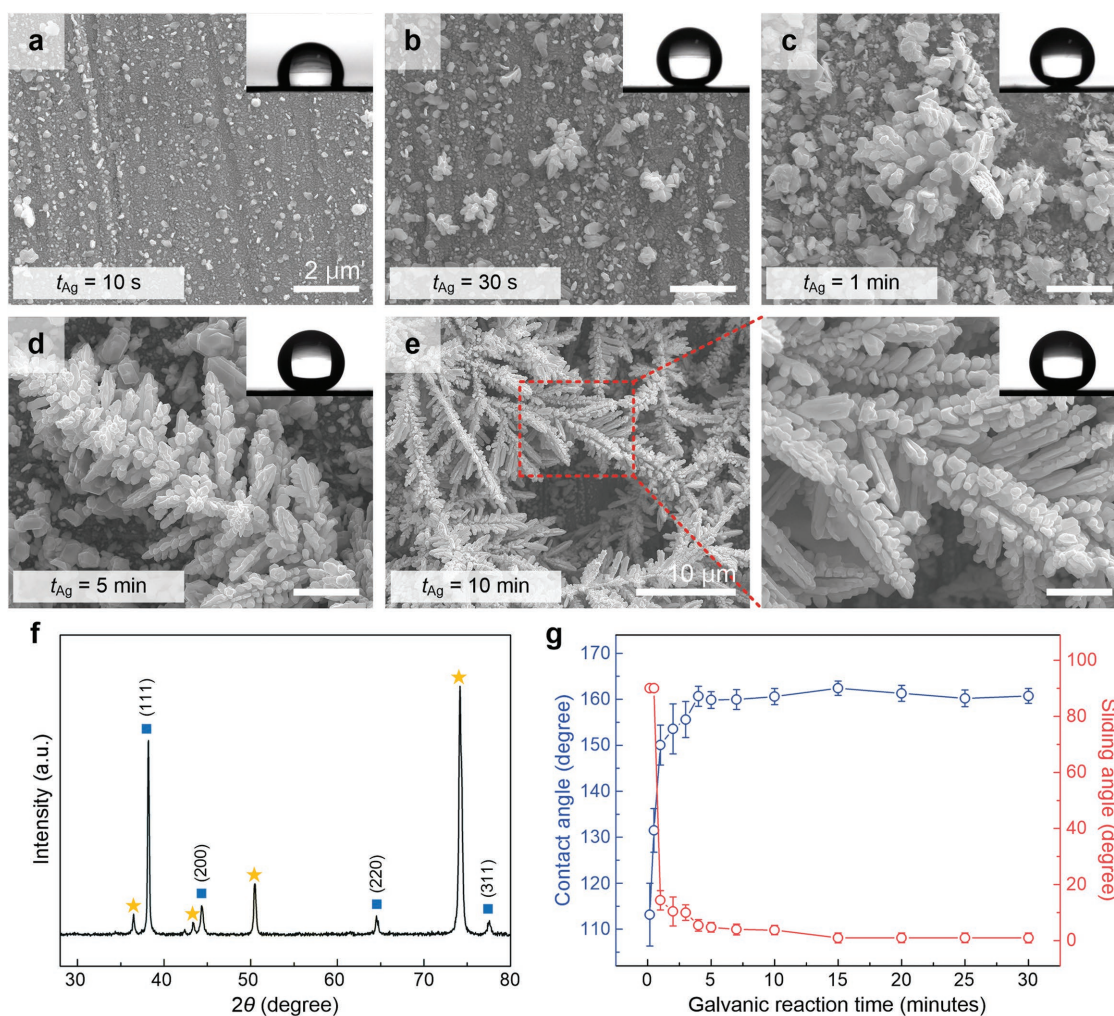


Figure 2. a–e) SEM images of Ag dendrites deposited on a Cu substrate as a function of increasing galvanic reaction time (t_{Ag}): a,b) Ag particle nucleation and deposition at t_{Ag} of 10 and 30 s, respectively. c,d) Ag dendrites with trunks and short branches at t_{Ag} of 1 min (scale bar: 2 μm). e) Fully grown hierarchical Ag dendritic structure composed of Ag nanoparticles, branches, and leaves at t_{Ag} of 10 min (scale bar: 10 μm) and the corresponding higher magnification image (scale bar: 2 μm). The insets show optical images of a 1 μL water droplet on each substrate. f) XRD spectra of the fully grown Ag dendritic structure on the Cu plate. g) Water contact angles (blue, left axis) and sliding angles (red, right axis) of 1 μL droplets on the substrate as a function of t_{Ag} .

at 43.36° , 50.48° , and 74.16° correspond to the (111), (200), and (220) planes of Cu fcc structures (JCPDS No. 04-0836). The composition of the as-prepared substrate was further examined by energy-dispersive spectroscopy (EDS) analysis, as shown in Figure S2 in the Supporting Information. The EDS analysis confirmed that Ag dendritic structures were successfully constructed on the surface of the Cu plate.

The inset images in Figure 2a–e and the data in Figure 2g show that the surface wetting properties of the PFDT-modified Ag dendritic substrates depend on the galvanic reaction time. The changes in the static water contact angles (CAs) and water sliding angles (SAs) with galvanic reaction time were determined to identify the surface wetting properties of the PFDT-modified Ag dendritic substrate, as shown in Figure 2g. After the initial reaction stage (galvanic reaction time of 10 s), the water CA was 113.2° and the droplet did not roll off, even when the surface was tilted vertically, indicating that the surface had insufficient surface roughness from Ag dendrites to obtain superhydrophobicity. Increasing the reaction time resulted in a drastic increase in the water CAs to 150° at a reaction time of 1 min, with saturation observed after 4 min. The water SAs also drastically decreased to less than 5° at a reaction time of 5 min, with saturation of the SA ($\approx 1^\circ$) observed after 10 min. The resulting superhydrophobic properties of the Ag dendritic substrate can be ascribed to the hierarchical micro-/nanoroughness of the Ag dendrites and decreased surface energy of the PFDT coating.^[24]

Therefore, the increase of the water CAs on the Ag dendritic structures was in good accordance with the SEM

images shown in Figure 2, which exhibited Ag dendritic substrates with increasing surface roughness as the galvanic reaction time increased. In addition, the extreme water-repellent characteristics of the PFDT-modified Ag dendritic substrate can be explained by the Cassie–Baxter wetting model.^[25] The details of the model are described in the Supporting Information.

To manipulate the movement of a droplet on the superhydrophobic Ag dendritic substrate, a droplet-guiding track was fabricated by sculpting a shallow groove into the Cu plate in advance of the galvanic displacement reaction (Figure 1a–i). The control of droplet motion, including moving and stopping, was achieved simply by locating a droplet stopper at the center of the guiding track. The droplet stopper was designed similar to a stair by creating depth differences in the center of the guiding track, as shown in Figure 3a. The SEM images in Figure 3b,c confirmed that Ag dendritic structures were successfully constructed on the surface of the Cu plate despite the presence of the droplet stopper in the guiding track. Although the Ag dendritic structures fully covered the surface of the droplet stopper, it maintained the original round-shaped structure. Owing to the highly water-repellent properties of the superhydrophobic Ag dendritic substrate, a water droplet could be easily rolled off the superhydrophobic substrate along the grooved guiding track without any loss of the droplet, despite the low tilt angle ($<2^\circ$). Moreover, it can be stopped by bumping against the droplet stopper, and resume movement after collision with an approaching droplet released at a later time.

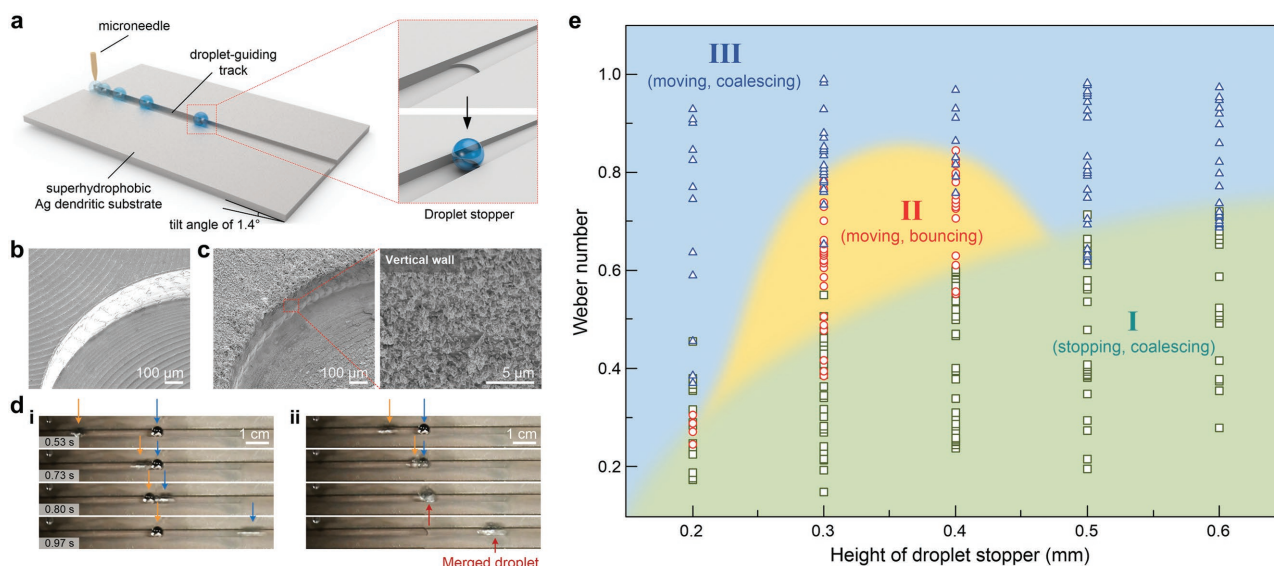


Figure 3. a) Schematic illustration of a droplet-guiding-track-engraved superhydrophobic Ag dendritic substrate with a droplet stopper at the center of the droplet-guiding track. SEM image of the droplet stopper located in the center of droplet-guiding track b) before and c) after constructing Ag dendritic structures via galvanic displacement reaction. The magnified image shows the vertical wall of the step at the channel. d) Time-sequential photographic images of colliding water droplets ($1 \mu\text{L}$) in the droplet-guiding track with a 0.3 mm high droplet stopper. When droplets collide with each other, (i) bouncing or (ii) coalescing collisions occurred. The orange and blue arrows indicate the newly dropped second droplet and the first droplet, respectively. The merged droplet after collision is marked with a red arrow. e) Experimentally determined collision regimes for water droplets on the droplet-guiding-track-engraved superhydrophobic Ag dendritic substrate with a droplet stopper. The three regions indicate three types of collision phenomena on the droplet-guiding track with various droplet stopper heights (0.2–0.6 mm at intervals of 0.1 mm). Squares (green region), circles (yellow region), and triangles (blue region) indicate type I (stopping, coalescing), type II (moving, bouncing), and type III (moving, coalescing), respectively, as a function droplet stopper height and Weber number.

Collisions between water droplets on a superhydrophobic surface can be classified as bounce or coalescence according to various physical parameters, including kinetic energy and collision geometry.^[26] For the superhydrophobic guiding track, the impact parameter, which is directly related to the collision geometry and defined as the perpendicular distance between the centers of two approaching droplets, can be assumed to zero due to the straight track of the substrate. Therefore, the collision phenomena are mainly dominated by the kinetic energy difference between the colliding droplets. In the guiding track with a droplet stopper, the collisions between droplets could also be affected by the height of the droplet stopper owing to its potential energy. A droplet stopper with a higher height requires a greater difference in the kinetic energies of the colliding droplets for a droplet to step over the droplet stopper. The time-sequential photographic images in Figure 3d show bouncing and coalescing collisions, respectively, of water droplets moving on the guiding track with a 0.3 mm high droplet stopper. In these images, the locations of the moving water droplets are indicated by orange and blue arrows. Various droplet collision phenomena were observed depending on the Weber number of the newly dropped droplet, which is a dimensionless parameter of kinetic energy. The Weber number, We , is defined as $We = 2\rho v^2 R/\gamma$, where v is velocity of a newly dropped droplet, R is the droplet radius, and ρ and γ are the density and surface tension of the liquid, respectively. Therefore, a large Weber number describes a large kinetic energy difference between colliding droplets. For example, the colliding droplets in Figure 3d-ii ($We = 0.84$) have a larger kinetic energy difference than those in Figure 3d-i ($We = 0.70$). The collision phenomena determined by the kinetic energy of the newly dropped droplet and potential energy of the droplet stopper could be classified as three types: (I) stopping of a merged droplet after a coalescing collision; (II) resumed moving of the first droplet and stopping of the newly dropped second droplet after a bouncing collision; (III) moving of a merged droplet after a coalescence collision. To realize a droplet-based real-time SERS sensor, the stable droplet bouncing region (type II) should be achieved. Figure 3e shows the experimentally determined collision regimes of water droplets on the guiding track with various droplet stopper heights (0.2–0.6 mm at intervals of 0.1 mm) with three regions indicating the three types of collision phenomena. The collision phenomena were observed in the order of type I (stopping, coalescing) to type II (moving, bouncing) to type III (moving, coalescing) as the kinetic energy of the newly dropped droplet increased for a given droplet stopper height. As shown in Figure 3e, the type II collision phenomenon was achieved for the broadest range of Weber numbers with a 0.3 mm high droplet stopper. More than 100 consecutive droplet manipulations were achieved under the type II conditions (see Movie S1 in the Supporting Information for more details). From these results, we could successfully demonstrate the droplet-based real-time SERS sensor under these conditions.

Figure 4a shows a schematic illustration of the droplet-based real-time SERS sensor, in which successive analyte droplets are moved along the guiding track and stopped at a laser spot for Raman excitation. Photographic images of the

droplet-based real-time SERS sensor with a static droplet at the laser spot are shown in Figure 4b. The SERS sensor has a simple structure and provides easy operation for droplet handling compared with conventional closed-channel microfluidic devices, which require several components, including pneumatic valves and pumps. In particular, static droplets on the sensor showed CAs of $>150^\circ$ without any shape deformation in the 2 mm wide confined track. The droplet has a completely spherical shape, which enables stable SERS measurements to be obtained. At this point, one issue that could be raised is that of droplet evaporation caused by laser irradiation during the SERS measurements, which should be avoided to prevent imprecise molecule analysis in the droplet-based SERS sensor. To address the aforementioned issue, the change in droplet volume was investigated by comparing the volume of droplets before and after laser irradiation. The time-dependent volume changes of the droplet in Figure S4 in the Supporting Information confirmed that the droplet loss was negligible levels of 2% under the laser irradiation time lower than 5 s. Therefore, we could expect that enrichment effects hardly occurred during the SERS measurement. Meanwhile, Ag dendritic substrates composed of randomly oriented nanoparticles, branches, and leaves are well known as effective SERS substrates owing to the huge amount of micro-/nanoscale structures of sharp edges and nanoscale junctions, resulting in a high potential for providing tremendous SERS hot spots.^[23,27–30] Therefore, stable SERS detection, as well as effective manipulation of droplets containing probing molecules, could be achieved using the droplet-based real-time SERS sensor.

To evaluate the SERS performance of the droplet-based real-time SERS sensor with respect to the surface morphology of the Ag dendritic substrate at various galvanic reaction times, SERS measurements were carried out using a 1 μL droplet containing 10^{-3} M R6G as a probing molecule. Figure 4c shows the variation in the Raman intensity at 1363 cm^{-1} , which is the highest intensity peak in the SERS spectrum of R6G, on the droplet-based real-time SERS sensor prepared with various reaction times: 2, 3, 5, 7, 10, 15, 20, and 25 min. As the excitation of localized surface plasmons strongly depends on the morphology of SERS-active metallic structures, a variation of SERS performance was observed with different reaction times. In our SERS sensor, the intensities increased as the reaction time increased from 2 to 5 min, and then decreased as the reaction time increased from 5 to 25 min. Because Ag nanostructures on the substrates mainly contribute to the localized surface plasmon excitation, leading to stronger Raman scattering, the results obtained for reaction times from 2 to 5 min are in good agreement with the morphology evolution of the Ag dendritic structures, as described in Figure 1c,d. However, at reaction times over 5 min, the size of the Ag dendritic structures increased and the surface of the structures became smooth through additional Ag deposition on the dendrites. Thus, excessive galvanic reaction induced a decrease in the density of SERS hot spots and degraded the SERS performance. On the basis of these results, we concluded that the optimal reaction time for fabricating our droplet-based real-time SERS sensor is 5 min.

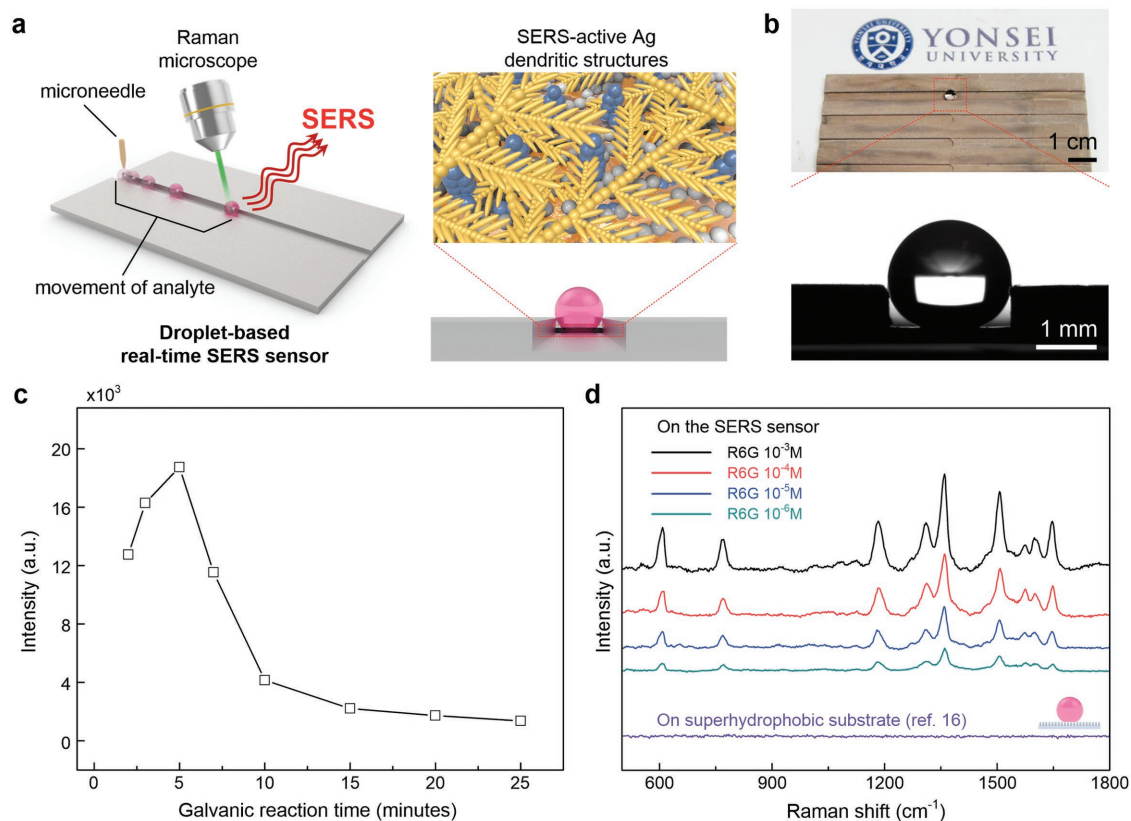


Figure 4. a) Schematic illustrations of the droplet-based real-time SERS sensor: An analyte droplet moves along the droplet-guiding track and stops at the Raman laser spot on the substrate covered with Ag-dendritic structures. b) Photographic images showing the high static water CAs at the laser spot without any shape deformation in the confined track with a width of 2 mm. c) Variation in the Raman intensity at 1363 cm⁻¹ corresponding to a SERS peak of R6G on the droplet-based SERS sensor with respect to t_{Ag} . d) SERS spectra of R6G-containing droplets (from top: 10⁻³, 10⁻⁴, 10⁻⁵, and 10⁻⁶ M) on the droplet-based SERS sensor and reference SERS spectrum (purple line, bottom) obtained on a superhydrophobic SERS-inactive substrate.

Finally, we obtained SERS spectra of droplets with various concentrations of R6G (10⁻³–10⁻⁶ M) on the optimized droplet-based real-time SERS sensor, as described in Figure 4d. All the obtained spectra clearly exhibited characteristic peaks of R6G molecules, such as C–C–C ring in-plane bending (612 cm⁻¹), C–H out of plane bending (773 cm⁻¹), aromatic C–H bending (1183 cm⁻¹), C–O–C stretching (1312 cm⁻¹), and aromatic C–C stretching (1363, 1511, 1575, and 1650 cm⁻¹).^[31] The intensities of the obtained Raman peaks decreased as the concentration of R6G in the probing droplet decreased (Figure S3 in the Supporting Information). Although low concentrations of probing molecules are difficult to detect under droplet conditions, the spectrum of the 10⁻⁶ M R6G droplet clearly exhibited the main Raman peaks. On the other hand, no peaks corresponding to R6G were observed on a superhydrophobic SERS-inactive substrate lacking Ag metallic nanostructures.^[16] From the obtained results with R6G droplets, the enhancement factor (EF) of our optimized droplet-based real-time SERS sensor was evaluated to be 6.3×10^5 , indicating that the SERS enhancement achieved with the droplet-based SERS sensor is comparable to that of conventional SERS-integrated closed-channel microfluidic devices.^[7] The details of the EF calculation are described in the Supporting Information.

To confirm that the droplet-based SERS sensor can be used as a real-time SERS substrate without any contamination from the probing molecule after the SERS measurement, successive SERS measurements were obtained with and without 10⁻⁶ M R6G droplets, as shown in Figure 5a. The three colored SERS spectra and four black lines indicate that successive and stable SERS measurements are achieved without any interference, suggesting that the superhydrophobic properties of the sensor prevent molecular contaminants. Figure 5b shows that the droplet-based real-time SERS sensor is sufficiently sensitive and reproducible, even after several times detection of a target analyte. The main Raman peaks in Figure 5b for a droplet containing 10⁻⁵ M NBA correspond well to those reported in the literature.^[32] Based on the excellent performance and reproducibility for different analytes, the droplet-based real-time SERS sensor could be used to detect various analytes on the same substrate without a cleaning process. MG- and NBA-containing droplets were alternately released at the end of the guiding track. As shown in Figure 5c, the alternating MG- and NBA-containing droplets were sequentially detected on the droplet-based real-time SERS sensor. The spectra clearly exhibited identical characteristic peaks of MG or NBA, without spectral interference that would be expected owing to surface contamination by the analytes.^[5] Therefore, our droplet-based real-time SERS

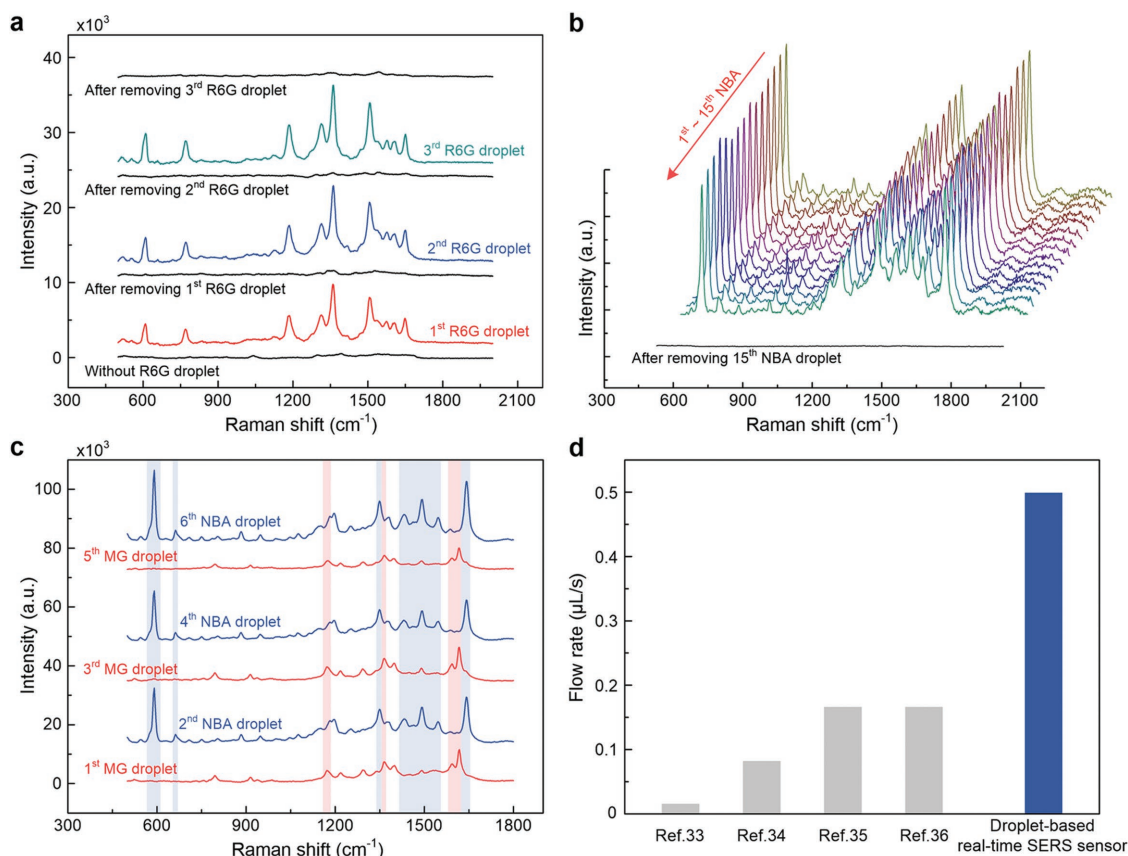


Figure 5. a–c) SERS spectra of droplets containing various probing molecules on the droplet-based real-time SERS sensor. SERS spectra of a) R6G-containing droplets (three colored lines) and b) NBA-containing droplets (fifteen colored lines) show successive and stable SERS measurements. The black lines show the reproducibility of the droplet-based SERS sensor. c) SERS spectra of the MG- and NBA-containing droplets obtained alternately at the same laser spot without spectral interference between the analytes. d) Comparison of the flow rate of the droplet-based real-time SERS sensor used for successive SERS measurement with those of conventional closed-channel microfluidic SERS sensors.

sensor can reduce the sample preparation time to a few seconds through simple analyte droplet replacement via the droplet collision mechanism, and enable successive SERS detection of various target analytes based on its high resistance to surface contaminants. Figure 5d shows the flow rate of the analyte droplet on our droplet-based real-time SERS sensor compared with those on conventional closed-channel microfluidic SERS sensors. On the droplet-based real-time SERS sensor, 1 μL droplets containing probing molecules were released at the end of the guiding track using a syringe pump with a rate of $0.5 \mu\text{L s}^{-1}$ and the droplets were easily stopped on the Raman laser spot, allowing SERS measurements to be obtained. In contrast, closed-channel microfluidic devices are typically operated at much lower flow rates of $\approx 0.2 \mu\text{L s}^{-1}$.^[33–36] Furthermore, the deposited droplet could be quickly replaced with the next analyte droplet for successive SERS measurements without a cleaning process. This result indicates that the droplet-based real-time SERS sensor based on the fast and easy manipulation of analyte droplets and successive SERS measurement is a promising microfluidic SERS sensor for high-throughput real-time SERS monitoring. We believe that this SERS sensor will be useful as an advanced high-throughput SERS platform for applications requiring fast detection of small volumes of analyte.

In addition, the droplet manipulation mechanism has strong merits that allow easy and rapid manipulation of successive droplets. As this technique adjusts the collision phenomena, it has a great potential in versatile applications as well as in SERS. The coalescing collisions enable homogeneous mixing of droplets containing different reactants, and hence, it can be used for chemical reactions such as nanoparticle synthesis and hydrogel crosslinking. Furthermore, the development of the multi-inlet-multi-outlet droplet-guiding track will extend the usability of the manipulation technique. Therefore, we foresee that further enhancement of the manipulation technique will bring great advantages in a wide variety of biological and chemical applications such as in situ monitoring of chemical reactions and high-throughput drug screening.

3. Conclusion

In summary, we developed a novel droplet-based SERS sensor for real-time SERS monitoring based on a superhydrophobic SERS-active Ag dendritic substrate. This substrate was obtained through a galvanic displacement reaction between Cu and Ag, and water-repellent properties were achieved using a PFDT coating. By designing the SERS sensor with

a shallow groove structure and a droplet stopper, the analyte droplet could be easily transported to the laser spot for SERS measurement and easily replaced by the next analyte droplet. On the optimized SERS sensor, an EF of 6.3×10^5 was obtained for droplets containing R6G as a probing molecule. The superhydrophobic properties and simple operation mechanism of the optimized SERS sensor enable successive droplet manipulation and SERS measurements without any surface contamination or a cleaning process. This novel droplet-based real-time SERS sensor could be regarded as an advanced SERS device for high-throughput, real-time biological and chemical molecular detection.

4. Experimental Section

Materials: CH_3COOH (20%) and silver nitrate (AgNO_3 , $\geq 98\%$) were purchased from Ducksan Pure Chemical. PFDT (97%), R6G, NBA, and MG were purchased from Sigma-Aldrich.

Fabrication of Droplet-Based Real-Time SERS Sensor: The droplet-based real-time SERS sensor was fabricated on a 1 mm thick Cu plate. To manipulate droplets on the Cu plate, the Cu plate was sculpted with a stair structure (width of 2 mm and step height of 0.3 mm) using a computer numerical control milling method. To fabricate SERS-active metallic nanostructure on the substrate, Ag dendritic structures were synthesized on the as-prepared Cu plate using a galvanic displacement reaction. The droplet-guiding-track-engraved Cu plate was subsequently cleaned with acetone, isopropyl alcohol, and deionized water to remove any organic contaminants. The cleaned Cu plate was dipped into a 20% CH_3COOH aqueous solution for 3 h at room temperature to remove copper oxide and residual contaminants. Subsequently, the Cu plate was immersed in an aqueous solution of 3×10^{-3} M AgNO_3 at room temperature for the galvanic displacement reaction. The Ag^+ ions dissolved in the solution were reduced and deposited on the Cu plate. Upon formation of Ag dendritic structures after a few minutes, the Ag-deposited Cu plate was dipped into a 1×10^{-3} M solution of PFDT in ethanol for 1 h to achieve surface modification in order to alter the wettability of the Ag dendritic structures from hydrophilic to hydrophobic.^[37] Then, the SERS-active Ag dendritic substrate was rinsed with ethanol to remove residual organic reactants. Finally, the substrate was dried under nitrogen flow and baked at 80 °C on a hot plate to obtain the superhydrophobic SERS-active substrate for the droplet-based real-time SERS sensor.

Droplet Manipulations on Droplet-Guiding Tracks: Droplet manipulations were investigated to find the droplet bouncing region with respect to the height of the droplet stopper for the droplet-based real-time SERS sensor. The Cu plates ($10 \times 3 \times 1$ mm) were prepared and sculpted with droplet-guiding tracks (2 mm width) and various heights of droplet stopper (0.2–0.6 mm at intervals of 0.1 mm). Specifically, the depth in front of the droplet stopper on the guiding track was 0.3–0.7 mm, and the depth to the rear of the droplet stopper was maintained at 0.1 mm. In the droplet manipulation experiments, the substrate was maintained at a tilt angle of 1.4° , a first 1 μL water droplet was placed in front of the droplet stopper, and a second 1 μL droplet was dropped at various sites in front of the droplet stopper within the guiding track using a microneedle in order to obtain different Weber numbers. The collision of water droplets was repeatedly performed using

various droplet stopper heights and droplet Weber numbers, and the droplet motions were recorded by a video camera (HDR-CX550, Sony Co., Ltd.) at 29 fps. To analyze the droplet collision process, the images were captured from the recorded videos and used to determine the Weber number of the manually dropped second droplet. The distances between the first and second droplets were measured using the ImageJ software in order to calculate the velocity of the second droplet and determine the Weber number. Finally, every droplet collision event was labeled with respect to the Weber number and height of the droplet stopper.

Characterization and SERS Measurement: The morphology and EDS elemental mapping of the Ag dendritic substrate were characterized using field emission scanning electron microscopy (JEOL JSM-7001F) at an acceleration voltage of 15 kV. The surface chemistry of the Ag dendritic substrate was analyzed using XRD spectroscopy (Rigaku D/MAX-2500H). The contact angles for 1 μL of deionized water on the substrate were determined using a contact angle analyzer (Phoenix 300, SEO Co. Ltd.). The release of 1 μL droplets was conducted using a syringe pump (NE-300, New Era Pump System, Inc.) with an 8 mm 31G needle (BD Ultra-Fine II, BD). In the SERS measurements, a Horiba Lab ARAMIS Raman spectrometer was used with an Ar^+ laser (5 mW and 514 nm) and a He–Ne laser (2 mW and 633 nm) as light sources. Droplets containing various concentrations of R6G (10^{-3} – 10^{-6} M) as a probing molecule were used to characterize the SERS performance of the droplet-based real-time SERS sensor using the He–Ne laser. For successive SERS measurements on the droplet-based real-time SERS sensor, droplets of 10^{-5} M NBA and MG were released to the laser spot at 1 s intervals, followed by SERS measurement using the Ar^+ laser. The integration times for R6G, NBA, and MG were 5 and 1 s, respectively. The excitation light was focused on the 1 μL droplet containing the probing molecule using a 10 \times microscope objective (Olympus). The excitation light was refocused on the surface of the droplet-based real-time SERS sensor after the SERS measurement to detect any residual contaminants. For the droplet evaporation experiment, the time duration of the 5 mW Ar^+ laser irradiation was 1 s with a duty cycle of 0.5.

Supporting Information

Supporting Information is available from the Wiley Online Library or from the author.

Acknowledgements

This work was supported by the Priority Research Centers Program (2012-0006689) through the National Research Foundation (NRF) of Korea funded by the Ministry of Education, Science and Technology (MEST) and Mid-Career Researcher Program through NRF grant funded by the MEST (2014R1A2A2A09053061), and the R&D program of MOTIE/KEIT [10064081, Development of fiber-based flexible multimodal pressure sensor and algorithm for gesture/posture-recognizable wearable devices]. This work was partially supported by the Yonsei University Future-leading

Research Initiative and Implantable artificial electronic skin for an ubiquitous healthcare system of 2016-12-0050.

- [1] B. Schrader, *Infrared and Raman Spectroscopy*, WILEY-VCH, Weinheim, Germany **1995**.
- [2] P. L. Stiles, J. A. Dieringer, N. C. Shah, R. P. Van Duyne, *Annu. Rev. Anal. Chem.* **2008**, *1*, 601.
- [3] W. E. Doering, S. Nie, *Anal. Chem.* **2003**, *75*, 6171.
- [4] S. Chan, S. Kwon, T.-W. Koo, L. P. Lee, A. A. Berlin, *Adv. Mater.* **2003**, *15*, 1595.
- [5] M. P. Cecchini, J. Hong, C. Lim, J. Choo, T. Albrecht, J. Andrew, J. B. Edel, *Anal. Chem.* **2011**, *83*, 3076.
- [6] J. Leem, H. W. Kang, S. H. Ko, H. J. Sung, *Nanoscale* **2014**, *6*, 2895.
- [7] H. Mao, W. Wu, D. She, G. Sun, P. Lv, J. Xu, *Small* **2014**, *10*, 127.
- [8] D. Ward, N. J. Halas, J. Ciszek, J. Tour, Y. Wu, P. Nordlander, D. Natelson, *Nano Lett.* **2008**, *8*, 919.
- [9] S. Wells, S. Retterer, J. Oran, M. Sepaniak, *ACS Nano* **2009**, *3*, 3845.
- [10] N. A. Abu Hatab, J. M. Oran, M. J. Sepaniak, *ACS Nano* **2008**, *2*, 377.
- [11] Q. Zhang, Y. H. Lee, I. Y. Phang, C. K. Lee, X. Y. Ling, *Small* **2014**, *10*, 2703.
- [12] B.-B. Xu, Z.-C. Ma, L. Wang, R. Zhang, L.-G. Niu, Z. Yang, Y.-L. Zhang, W.-H. Zheng, B. Zhao, Y. Xu, Q.-D. Chen, H. Xia, H.-B. Sun, *Lab Chip* **2011**, *11*, 3347.
- [13] B.-B. Xu, R. Zhang, X.-Q. Liu, H. Wang, Y.-L. Zhang, H.-B. Jiang, L. Wang, Z.-C. Ma, J.-F. Ku, F.-S. Xiao, H.-B. Sun, *Chem. Commun.* **2012**, *48*, 1680.
- [14] S. M. Kang, I. You, W. K. Cho, H. K. Shon, T. G. Lee, I. S. Choi, J. M. Karp, H. Lee, *Angew. Chem. Int. Ed.* **2010**, *49*, 9401.
- [15] I. You, S. M. Kang, S. Lee, Y. O. Cho, J. B. Kim, S. B. Lee, Y. S. Nam, H. Lee, *Angew. Chem. Int. Ed.* **2012**, *51*, 6126.
- [16] J. Seo, S.-K. Lee, J. Lee, J. Seung Lee, H. Kwon, S.-W. Cho, J.-H. Ahn, T. Lee, *Sci. Rep.* **2015**, *5*, 12326.
- [17] S. Shin, J. Seo, H. Han, S. Kang, H. Kim, T. Lee, *Materials* **2016**, *9*, 116.
- [18] X. Xia, Y. Wang, A. Ruditskiy, Y. Xia, *Adv. Mater.* **2013**, *25*, 6313.
- [19] C. Gu, H. Ren, J. Tu, T.-Y. Zhang, *Langmuir* **2009**, *25*, 12299.
- [20] X. Xu, Z. Zhang, J. Yang, *Langmuir* **2010**, *26*, 3654.
- [21] G. Zhang, S. Sun, M. N. Banis, R. Li, M. Cai, X. Sun, *Cryst. Growth Des.* **2011**, *11*, 2493.
- [22] D. Kim, J. Seo, S. Shin, S. Lee, K. Lee, H. Cho, W. Shim, H. B. R. Lee, T. Lee, *Chem. Mater.* **2015**, *27*, 4964.
- [23] W. Cai, X. Tang, L. Yang, X. Wang, *Mater. Res. Bull.* **2013**, *48*, 4125.
- [24] D. Quéré, *Annu. Rev. Mater. Res.* **2008**, *38*, 71.
- [25] A. B. D. Cassie, S. Baxter, *Trans. Faraday Soc.* **1944**, *40*, 546.
- [26] H. Mertaniemi, R. Forchheimer, O. Ikkala, R. H. A. Ras, *Adv. Mater.* **2012**, *24*, 5738.
- [27] A. Gutés, C. Carraro, R. Maboudian, *J. Am. Chem. Soc.* **2010**, *132*, 1476.
- [28] F. Jiang, S. Wang, L. Li, H. Jin, W. Zhang, J. Lin, T. Tang, J. Wang, *Green Chem.* **2011**, *13*, 2831.
- [29] H. B. Li, P. Liu, Y. Liang, J. Xiao, G. W. Yang, *Nanoscale* **2012**, *4*, 5082.
- [30] Z. Yi, X. Tan, G. Niu, X. Xu, X. Li, X. Ye, J. Luo, B. Luo, W. Wu, Y. Tang, Y. Yi, *Appl. Surf. Sci.* **2012**, *258*, 5429.
- [31] J. Lee, J. Seo, D. Kim, S. Shin, S. Lee, C. Mahata, H.-S. Lee, B.-W. Min, T. Lee, *ACS Appl. Mater. Interfaces* **2014**, *6*, 9053.
- [32] C. Li, Ö. Dag, T. D. Dao, T. Nagao, Y. Sakamoto, T. Kimura, O. Terasaki, Y. Yamauchi, *Nat. Commun.* **2015**, *6*, 6608.
- [33] L. Wu, Z. Wang, S. Zong, Y. Cui, *Biosens. Bioelectron.* **2014**, *62*, 13.
- [34] R. Gao, N. Choi, S.-I. Chang, E. K. Lee, J. Choo, *Nanoscale* **2014**, *6*, 8781.
- [35] T.-H. Xia, Z.-P. Chen, Y. Chen, J.-W. Jin, R.-Q. Yu, *Anal. Methods* **2014**, *6*, 2363.
- [36] C. Fu, Y. Wang, G. Chen, L. Yang, S. Xu, W. Xu, *Anal. Chem.* **2015**, *87*, 9555.
- [37] J. Seo, S. Lee, H. Han, Y. Chung, J. Lee, S. D. Kim, Y. W. Kim, S. Lim, T. Lee, *Thin Solid Films* **2013**, *527*, 179.

Received: August 27, 2016
Revised: October 21, 2016
Published online: December 5, 2016